HAL
open science

Biaxial loading of arterial tissues with 3D in situ observations of adventitia fibrous microstructure: a method coupling multi-photon confocal microscopy and bulge inflation test

Cristina Cavinato, Clementine Helfenstein-Didier, Thomas Olivier, Sabine Rolland Du Roscoat, Norbert Laroche, Pierre Badel

To cite this version:

Cristina Cavinato, Clementine Helfenstein-Didier, Thomas Olivier, Sabine Rolland Du Roscoat, Norbert Laroche, et al.. Biaxial loading of arterial tissues with 3D in situ observations of adventitia fibrous microstructure: a method coupling multi-photon confocal microscopy and bulge inflation test. Journal of the mechanical behavior of biomedical materials, 2017, 10.1016/j.jmbbm.2017.07.022 . hal-01566802

HAL Id: hal-01566802

https://hal.science/hal-01566802

Submitted on 21 Jul 2017

HAL is a multi-disciplinary open access archive for the deposit and dissemination of scientific research documents, whether they are published or not. The documents may come from teaching and research institutions in France or abroad, or from public or private research centers.

L'archive ouverte pluridisciplinaire **HAL**, est destinée au dépôt et à la diffusion de documents scientifiques de niveau recherche, publiés ou non, émanant des établissements d'enseignement et de recherche français ou étrangers, des laboratoires publics ou privés.

Biaxial loading of arterial tissues with 3D *in situ* observations of adventitia fibrous microstructure: a method coupling multi-photon confocal microscopy and bulge inflation test

Cristina Cavinato[1, 2, 3], Clementine Helfenstein-Didier[1, 2, 3], Thomas Olivier[4], Sabine Rolland du Roscoat[5], Norbert Laroche[2], Pierre Badel[1, 2, 3]

[1]Ecole Nationale Supérieure des Mines de Saint-Etienne, CIS-EMSE, SAINBIOSE, F-42023 Saint-Etienne, France

[2]INSERM U1059, SAINBIOSE, F-42023 Saint-Etienne, France

[3]Université de Lyon, F-69000 Lyon, France

[4]Laboratoire Hubert Curien, UMR CNRS 5516, University of Lyon, France

[5]Laboratoire Sols, Solides, Structures, Risques (3SR), CNRS, UMR 5521, Université de Grenoble Alpes, G-INP, Grenoble, France

Corresponding author: Cristina Cavinato
École nationale supérieure des mines de Saint-Étienne
158 Cours Fauriel,
42023 Saint-Étienne France
E-mail: cristina.cavinato@emse.fr
Phone: +33 4 77 42 66 46

Keywords: Aorta; Thoracic aneurysm; Bulge inflation test; Collagen fibers; Orientation evolution

Word count: 6137 (introduction through conclusion)

Abstract (257 words)

Disorders in the wall microstructure underlie all forms of vascular disease, such as the aortic aneurysm, the rupture of which is necessarily triggered at the microscopic level. In this context, we developed an original experimental approach, coupling a bulge inflation test to multiphoton confocal microscopy, for visualizing the 3D micro-structure of porcine, human non-aneurysmal and aneurysmal aortic adventitial collagen under increasing pressurization. The experiment complexity on such tissues led to deeply address the acquisition major hurdles. The important innovative features of the methodology are presented, especially regarding region-of-interest tracking, definition of a stabilization period prior to imaging and correction of z-motion, z being the objective's axis. Such corrections ensured consistent 3D qualitative and quantitative analyses without z-motion. Qualitative analyses of the stable 3D images showed dense undulated collagen fiber bundles in the unloaded state which tended to progressive straightening and separation into a network of thinner bundles at high pressures. Quantitative analyses were made using a combination of weighted 2D structure tensors and fitting of 4 independent Gaussian functions to measure parameters related to straightening and orientation of the fibers. They denoted 3 principal fibers directions, approximately 45°, 135° and 90° with respect to the circumferential axis in the circumferential-axial plane without any evident reorientation of the fibers under pressurization. Results also showed that fibers at zero-pressure state were straighter and less dispersed in orientation for human samples – especially aneurysms – than for pigs. Progressive straightening and decrease in dispersion were quantified during the inflation. These findings provide further insight into the micro-architectural changes within the arterial wall.

1. Introduction

The aortic wall is a composite structure, made up of three different layers of heterogeneous nature—adventitia, media and intima—which enables its fundamental physiological functions. The

mechanical properties of this tissue have strong associations with the morphological properties of the underlying fibrous network (Gasser et al., 2006; Hemmasizadeh et al., 2015; Holzapfel et al., 2000).

An extensive amount of works available in the literature proves the increased interest of researchers on the bio-mechanical characterization of arterial tissue, particularly in the cause of traumatic aortic injuries and diseases, e.g., aneurysms and dissections. If on the one hand we can find many phenomenological constitutive models for modeling arterial wall mechanics, on the other hand there are other models based on various assumptions on deformation micro-mechanisms. These assumptions are often not fully verified and therefore controversial. An example is the typical question on affine or non-affine re-orientation of fiber bundles in arterial soft tissues (Chandran el al., 2006). The same problem and same open question should arise for rupture mechanisms that are triggered at the local scale. It is known that aneurysm formation is associated with a degeneration of the aortic extracellular matrix composition and architecture (Iliopoulos et al., 2009; Tsamis el al., 2013) but there are, so far, incomplete information, though they represent crucial information to understand aneurysm rupture and guide the decision-making in clinical diagnosis and treatment.

This context justifies the need to develop new experimental techniques which will pave the way for future research. These approaches should be dedicated to local scale observations and descriptions of the microstructure of vascular tissues. Among such experimental approaches, it is recognized that the correlation between mechanical function and microstructure of arteries can only be understood in the context of the three-dimensional imaging (O'Connell et al., 2008). X-ray computed microtomography is an interesting tool that can be used to obtain intermediate scale observations (Walton et al., 2015) and could be coupled with in situ mechanical testing (Helfenstein-Didier et al., 2016). However, it requires the use of contrast agents which may alter the mechanical behavior of the sample and certain precautions against radiation damage effects are needed.

For more refined, more local characterization and the least destructive effects, multi-photon confocal microscopy (MCM) is currently the most promising technique. This high resolution imaging technique allows a detailed observation of microstructural components which are thought to be most relevant for the mechanics of the tissue, namely collagen and elastin. Collagen is a source of second-harmonic generation (SHG) and intrinsic two photon fluorescence (TPF) signals; elastin is a significant source of extracellular matrix TPF (Koch et al., 2014). The coupling of the two signals constitutes the potential of MCM as a non-invasive technique for the characterization of arterial tissues. Multi-photon microscopy offers the advantage of being able to penetrate through the tissue depth displaying collagen and elastin separately without the necessity of tissue-preprocessing. It was applied in different experimental studies presented in recent years. The main concern was to describe the microstructure of the arterial wall (Niestrawska et al., 2016; Rezakhania et al., 2012; Schriefl et al., 2013) as well as describing some microstructural deformation mechanisms and fiber kinematics (Chow et al., 2014; Krasny et al., 2017; Sugita and Matsumoto., 2016; Schrauwen et al., 2012; Spronck et al., 2016). Though they demonstrated the potential of the technique, only a very limited number of specimens were studied in these pioneering works. Additionally, in thick specimens like human arteries and without any chemical or mechanical modifications, the main drawback of the microscopy technique is that the limited depth of observation only permits imaging of the adventitial layer.

Taking advantage of this limitation, the present work will focus on deformation mechanisms of the adventitial layer which is known to be the last barrier to overstretching and rupture (Duprey et al., 2016; Iliopoulos et al., 2009), hence a fundamental role in arterial mechanics. Accordingly, the goal of the present study is to develop a new experimental approach based on a bulge inflation test to study deformation micro-mechanisms in pressurized arterial (aneurysmal) tissues. A bulge inflation test is a technique that allows the study of biaxial mechanical behavior, which has already been used recently for investigations of porcine and human aortae (Marra et al., 2006; Mohan et al.,

1983), also in the case of aortic aneurysms (Romo et al., 2014; Trabelsi et al., 2015). It is an alternative method of planar biaxial loading that provides a closer mimicking of the *in vivo* loading states. Moreover the obtained results are less dependent on the method to clamp the specimens. The main objective of this approach was to provide biaxial loading conditions close to *in vivo* conditions for aneurysms, and to track a specific region of interest (ROI) during deformation.

In this paper, we present the details of the technique and its developments, based on histologically and clinically measurable data, and characterize morphological descriptors of the adventitial fibrous structure and their evolution.

2. Materials

2.1. Specimens preparation

Three different types of specimen were included in this study.

Porcine whole aortae (n = 9) were collected at a local slaughterhouse from domestic pigs aged 6-12 months. They were extracted carefully, removing surrounding connective tissue around the segments, within 12 h after the death. Before dissecting, the external diameter of the aorta was measured in different zones using a digital caliper. Aortae were cut open along the longitudinal direction, following the line of the intercostal arteries. 45-mm-square specimens were cut. The edges were parallel to the longitudinal and circumferential direction of the aortic tube.

Fresh non-aneurysmal human aortae (n = 2) were collected through the French voluntary body donation program from the Department of Anatomy of the University of Saint-Etienne. Under the same procedure used with porcine specimens, human specimens were dissected, within 12 h after the death.

Unruptured human ascending thoracic aortic aneurysms (ATAA) (n = 6) were collected from patients undergoing elective surgery to replace the segment with a graft, and underwent the same procedure again. The collections and the experiments on the specimens are done in accordance with

a protocol approved by the Institutional Review Board of the University Hospital Center of Saint Etienne.

Specimens (Fig. 1) were classified as segments of ascending thoracic part (AT) or descending thoracic part (DT). The thickness of each specimen was measured in 5 different positions using the digital caliper. Two plastic plates were used as external supports for the measurement. Table 1 gives the details of all tested specimens. After excision, the specimens were placed in PBS and refrigerated at 4°C during a maximum period of 12 h.

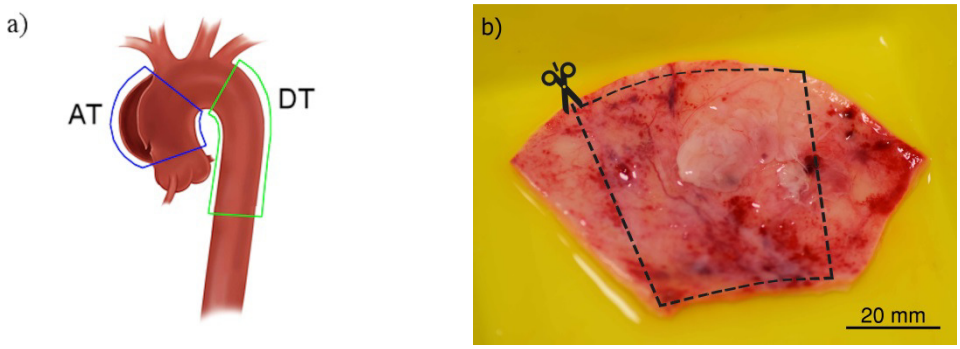

Fig. 1 (a) Classification in four different segments: ascending thoracic part (AT) and descending thoracic part (DT). (b) Example of a segment classified as AT, cut open in order to section the depicted 45-mm-square.

Specimens were clamped by gluing with ethyl cyanoacrylate the external edges of the adventitial side on a 30-mm-diameter PVC support, appendage of the inflation device. For the purpose of ROI tracking under the microscope during inflation, the center position of the mounted specimen was marked with a fluorescent micro particle. The dot consisted of a water-insoluble compound of Picro Sirius Red staining 1% w/v (50%) and ethyl cyanoacrylate (50%) which was placed by using a microneedle. The maximum radius in the axial-circumferential plane was about 300 µm and in the radial direction, the particle was confined to the outermost part of the tissue, corresponding to a single layer of imaged collagen fibers at the most.

Table 1 Data from collected specimens. Abbreviations: P=porcine, H=non-aneurysmatic human, AH=aneurysmal human.						
No. specimen	Tissue type	Anatomical position	Sex/age	Ex vivo segment diameter [mm]	Ex vivo thickness [mm]	Inflation pressure level [mmHg]
1	P	DT	NA	19.9	1.94	50/150/250/350/500
2	P	DT	NA	27.3	2.02	50/150/250/350/500
3	P	DT	NA	21.9	1.88	50/150/250/350/500
4	P	DT	NA	21.7	1.81	0/200/450
5	P	DT	NA	25.6	1.95	0/200
6	P	DT	NA	20.3	1.62	0/200/450
7	P	DT	NA	28.5	1.97	0/200/450
8	P	DT	NA	19.7	1.48	0/200/450
9	P	DT	NA	23.9	2.21	0/200
10	H	DT	F/92	22.2	2.27	0/200/450
11	H	DT	M/71	21.0	2.23	0/200
12		DT		19.7	2.08	0/200/450
13	AH	AT	M/69	52.1	2.11	0/200/450
14	AH	AT	M/51	57.6	1.94	0/200/450
15	AH	AT	F/55	55.7	1.91	0/200/450
16	AH	AT	M/44	57.1	1.95	0/200
17	AH	AT	M/48	49.2	2.57	0/200
18	AH	AT	F/61	51.2	1.81	0/200

2.2. Bulge inflation testing protocol

Clamping was achieved by aligning and gluing the intimal side of the specimen to a second PVC support and assembling and tightening the device. In this way the adventitial surface was exposed and a hermetic closure was ensured on the intimal surface (Fig. 2).

The circular exposed area of the adventitial surface was covered with PBS and remained immersed throughout the test duration. Inflation of the specimen was performed with an automatic water pumping system (WPI®, NE-501 Multi-Phaser) and a program developed in LabVIEW which controlled the injected volume at a constant rate. Pressure values were recorded simultaneously by a pressure transducer (Omega®). The inflation was performed injecting water at a constant rate of 2

mL/min. Then it was stopped, and the volume was kept constant, when specific levels of pressure showed in Table 1 were reached.

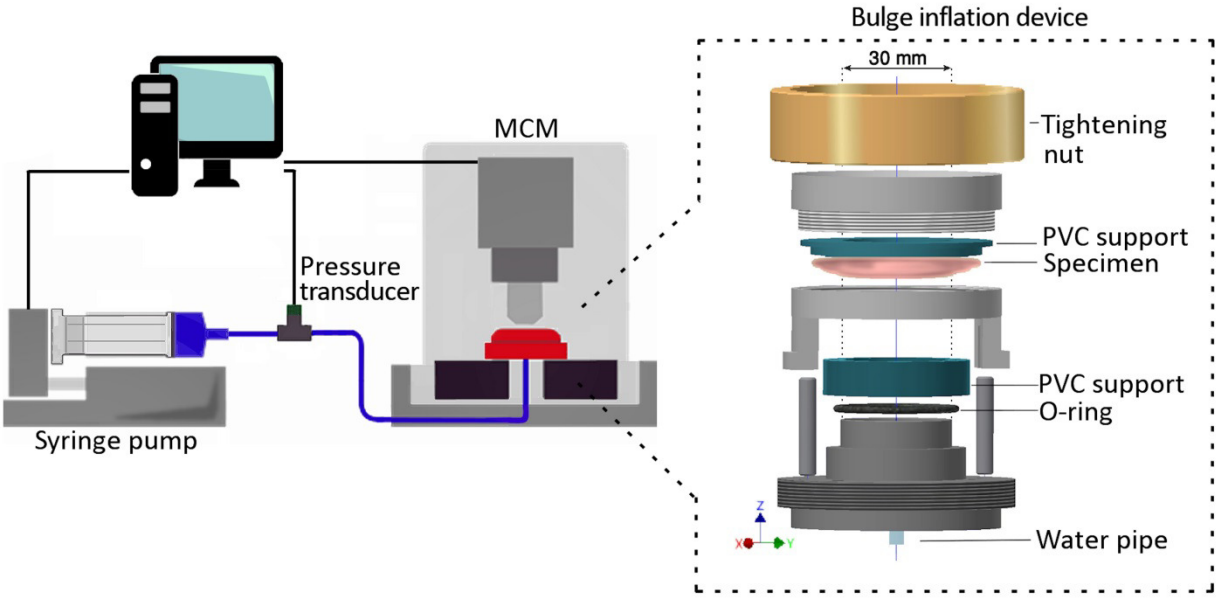

Fig. 2 Experimental setup used to associate the bulge inflation testing device to the MCM for visualizing the 3D microstructure at different pressures. The bulge inflation device is shown in a disaggregated configuration.

A preliminary study of relaxation-related behavior of the inflated sample was performed outside the MCM environment. Other porcine specimens (n = 4) were inflated similarly to the protocol detailed above, but using a constant rate of 30 mL/min and stopping at levels of 50, 150, 250, 350 and 500 mmHg. For each pressure level, the water volume was kept constant for at least 1 h, while pressure was recorded to assess stability of the sample configuration and decide when MCM acquisition should be performed. For this purpose each relaxation curve was fitted with a curve exponential decay equation, used to determine the necessary stabilization period prior to MCM imaging:

Equation 1

$$P(t) = P_0 exp\{-t/\tau\}$$

P is the generic state of pressure as function of time, P0 is the initial pressure and τ is the mean lifetime of the exponential decay. We specifically examined the value of the mean lifetime (Equation 1), useful as it can be interpreted as the time needed to reach a decay of 63% of the initial pressure.

The specific inflation pressures inside the MCM environment of 200 and 450 mmHg have been chosen for the purposes of evaluating a wall stress state (~120 mmHg) close to diastolic-systolic conditions and a second state beyond the physiological range. In fact, using the Laplace law and assuming as first reasonable approximations a hemispherical shape for both the aneurysm *in vivo* and the *in situ* specimen during the inflation, as well as a cylindrical shape for the normal vessel, the following equations shall apply:

Equation 2

$$P_a = \frac{P_s R_s}{R_a}, \qquad P_v = \frac{P_s R_s}{2\, R_v}$$

where P_s and R_s are the transmural pressure and the radius of the inflated specimens, and P_a, R_a, P_v, R_v are the transmural pressure and the radius of the aneurysm (a) and the normal vessel (v). This calculation is based on the assumption of a pure membrane behavior of the studied tissue during the inflation process, previously verified by Romo et al. (2014).

Given that R_s is close to 18 mm during the experiment and assuming an aneurysm radius of 30 mm and a normal vessel radius of 15 mm, inflation pressures of 200 and 450 mmHg correspond to *in vivo* pressures of 120 and 270 mmHg. The diastolic and systolic pressures of a healthy aorta are 80 and 120mmHg (Länne et al., 1992).

2.3. Multi-photon confocal microscopy protocol

Multiphoton microscopy images of the inflating specimens have been carried out with a LEICA TCS SP2 upright confocal microscopy system equipped with a water immersion objective (HCX

APO L UVI ×20 NA0.5). The laser source was a Ti:Sapphire femtosecond laser Chameleon Vision I from COHERENT, Inc. The excitation wavelength was set to 830 nm providing the best compromise between SHG signal and TPF signal on this setup. The detector dedicated to the SHG signal collected light between 375 and 425 nm. The detector dedicated to the TPF signal collected light between 560 and 700 nm. These conditions are similar to those found in other studies on comparable specimens (Boulesteix et al., 2006). The scanned volume was 750 × 750 × dz μm^3. The z-dimension dz could vary with the permeability of the sample to the pulsed laser beam approximately between 100 and 500 µm. All the specimens were used for the inflation bulge test coupled with the MCM imaging. At each pressure level, two scans were performed, after stabilization (see section 2.2), to obtain one stack of images 750 µm away from the fluorescent marker and one adjacent stack 1.4 mm away from it. This allowed obtaining images of a wider area. Each MCM scan had a 1024 × 1024 pixels numerical resolution, a 12 bit-dynamic range and a z-step of 1 µm, with 2-lines averaging at each z-step (meaning that each line was scanned 2 times and the 2 scans of each pixel were averaged).

To finely correct a part of the remaining z-motion due to possible small motions during acquisition of MCM stacks (lasting 15–30 min), two quasi-instantaneous scans (QI scans) with a z-step of 15 µm (5 s with only 10 slices) were performed immediately before and immediately after each principal scan. The goal of these QI scans was to provide data to determine the z-correction balancing possible z-motion during the acquisition of the normal scan. A custom MATLAB program based on image correlation was developed for this purpose (see Section 2.5.1). Then inflation was resumed up to the next threshold. A continuous time-imaging was adopted during the time intervals in which the inflated volume changed and during the stabilization periods. A group of fibers lying on the same focal plane was followed during the entire acquisition, thereby allowing to double check that the same ROI was tracked under the microscope.

2.4. Histology

Histological cross-sections of aortic specimens were prepared for the purpose of global morphological measurements and to assess structural effects of the tracking technique with ethyl cyanoacrylate and Picro Sirius Red. Two specimens of human aorta were dissected from remaining tissue of specimen no. 11. The overall dimensions were 10 mm × 20 mm. An axial line of Picro Sirius Red staining 1% w/v and ethyl cyanoacrylate was drawn with the tip of a needle on the adventitia surface of one of the human specimen which was left exposed at the compound for 2 h at 4°C. Then the two specimens were fixed with formaldehyde for 48 h, dehydrated in acetone for 48 h, embedded in methyl methacrylate (MMA) and sectioned in 9 µm slices in the circumferential-radial plane. Three-dimensional images of the slices were acquired with the multi-photon confocal microscope with a magnification of 40x.

2.5. Images processing and analysis

In addition to qualitative observations, a set of quantitative data was extracted from the obtained images. The steps performed are described below. To start processing the multi-photon images of elastin and collagen, a custom MATLAB tool was developed. Information for SHG was saved in channel 0 and information for TPF was saved in channel 1.

2.5.1. Z-motion correction

Because the image quality requires an acquisition time that cannot be neglected and, furthermore because some data were analyzed as a function of the z-coordinate, a precise correction of possible mechanical movements within the 3D stack of images in this direction was essential. For each normal stack of images, two quasi-instantaneous (QI) stacks were available. The interslice distance of the QI stacks was considered unalterable, since the acquisition time was minimized and the movement of the tissue during these acquisitions could be neglected. A set of operations based on

the calculation of intercorrelation coefficients between each image of each pair of stacks was used for comparing the three stacks and establishing the corrected value of the interslice distance in the normal stack. The details and a schematic of this method are presented in Appendix A (a successful validation study of the method was performed using both virtual images and actual images (results not shown here)). The percentage change between the estimated interslice distance of each normal stack and the theoretical interslice distance, corresponding to the z-step of 1 µm, was thus computed.

2.5.2. Planar orientation assessment of collagen fibers

In order to assess structural evolutions of the fibrous structure of adventitia under bulge inflation, it was decided to focus on the orientation distribution of the collagen fibrous network in the axial-circumferential plane. Taking into account previous observations of our stacks in the radial direction (results not shown here), fiber exhibited practically planar orientation in the axial-circumferential plane, in good agreement with other studies (Rezakhaniha et al., 2012), Thus, the planar orientation distribution function of the collagen fibers was estimated using the OrientationJ plugin for ImageJ software. This plugin is based on the computation of grey scale gradients and their related weighted 2D structure tensors at each pixel of a given slice, as described in Rezakhaniha et al. 2012. The structure tensor was computed with a Gaussian window of 3 pixels using a finite difference interpolation (Püspöki et al., 2016). Two isotropic properties resulting from the structure tensor, namely energy and coherency, were used to separate significant and negligible oriented area. Such a distinction was made by taking into consideration pixels which had at least 3% and 15% of normalized energy and coherency, respectively, which provided a good compromise between an adequate number of usable pixels and the neglect of insignificant information in our images. A weighted orientation histogram was built for each slice, discarding pixels below these thresholds. A representation of the orientation as a function of the depth z was

proposed to assess orientation characteristic changes through the thickness of the specimen at different pressures. The histogram was created after dividing all distribution values by the maximum value within the stack.

The average orientation was also calculated for each pressure level in a specimen by averaging all individual histograms and then averaging the result of the two adjacent stacks. The resultant histogram was normalized with respect to the total area, and then the relative distribution was used to fit 4 independent Gaussian functions, which were found to be appropriate for our data:

Equation 3

$$y(\theta) = y_b + \sum_{i=1}^{4} y_i(\theta) = y_b + \sum_{i=1}^{4} y_{p_i} \exp\left\{-\frac{(\theta-\theta_{m_i})^2}{2\,\sigma_i^2}\right\} \qquad 0° \leq \theta < 180°$$

where y_b is the base value, $y_i(\theta)$ is the contribution of each family, θ_m is its mean orientation, with standard deviation σ and maximum peak y_p (Fig. 3). The data-fitting was computed with a nonlinear least-squares solver, taking into account the continuity between 180° and 0°. Two indices characterizing the morphology of the fibrous structure were derived for each stack from the function $y(\theta)$:

Equation 4

$$\text{Alignment Index (AI)} = \sum_{i=1}^{4} \frac{y_{pi}}{\sigma i}$$

Equation 5

$$\text{Dispersion index \% (DI)} = \frac{180\ y_b}{\int_0^{180} y(\theta)d\theta} 100$$

The Alignment index characterizes the straightness of fibers, considering the dispersion of the families' orientation around their mean values θ_{m_i}. The narrower the orientation peaks, the higher the index. The Dispersion index denotes the contribution of the base value to the total distribution, hence the extent to which the fibers are evenly spread over the orientation range.

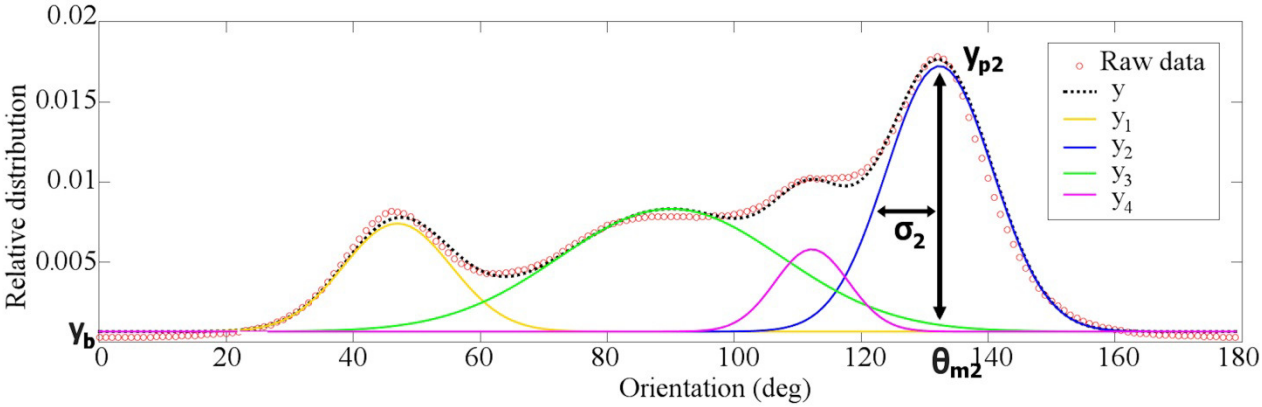

Fig. 3 Representative normalized orientation histogram and relative fit with a Gaussian function y representing 4 families of fibers, $y_{1\text{-}4}$. From the fitting, specific parameters denote the basic characteristics of each family of fiber: average orientation θ_m, peak height y_p, standard deviation σ, and the base value y_b of the distribution.

The four orientation families in a stack were ranked by calculating their respective contribution to the global distribution, computed as the ratio between the area under the individual curve yi(θ) and the area under the curve y(θ).The variation of these values during pressure increase was considered. TPF signal was not used for elastin orientation assessment because qualitative observations demonstrated low proportion of elastin, resulting in signal mostly from the low auto-fluorescence of collagen (Voytik-Harbin et al., 2001).

3. Results

3.1. Protocol adjustment

Fig. 4 shows two cross-section images of a histological slice of human descending segment observed with MCM and optical microscope to assess the influence of our marking technique. In the second case the adventitia surface was covered with a layer of the compound of Picro Sirius Red staining and ethyl cyanoacrylate 2 h before the histological process. The marked region was not recognizable in the images. In fact, no consistent difference with the previous observation was found in thickness of adventitia and structural appearance of fibers compared to areas far from the marked surface. It was considered that this marking technique is suitable for our purpose.

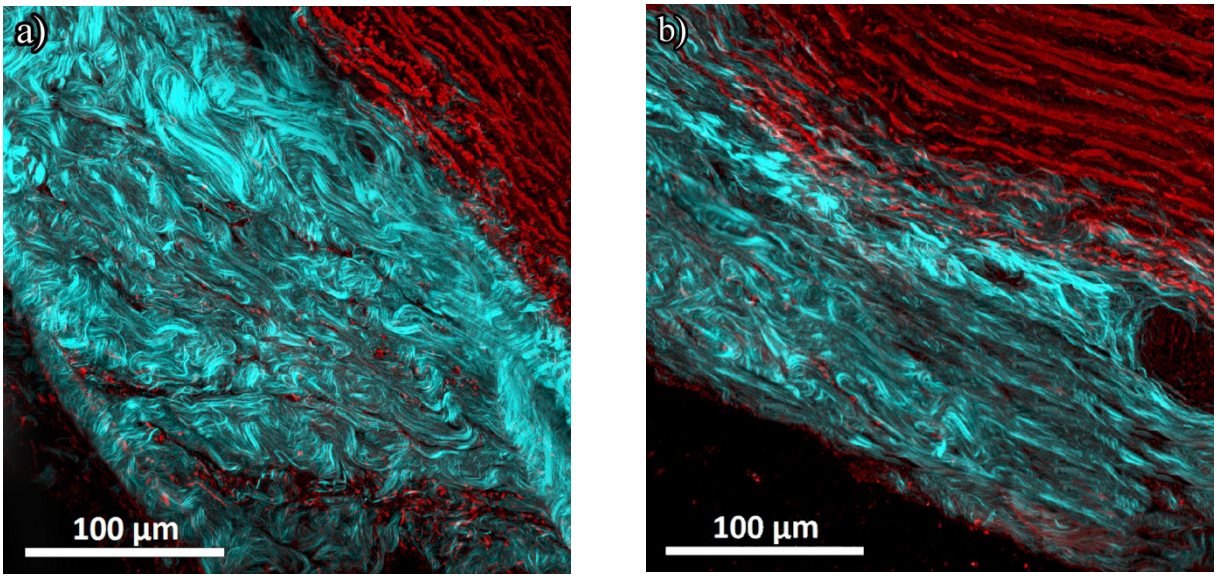

Fig. 4 Matrix architecture of two specimens of human descending thoracic aorta at the interface between adventitia and media. Representative MCM projections in the circumferential-radial plane. The unmodified specimen (a) and the specimen that has been marked with the Picro Sirius Red compound (b). Collagen and elastin are indicated in pale blue and red, respectively. (For interpretation of the references to color in this figure legend, the reader is referred to the web version of this article.)

As a second adjustment of our protocol, four porcine specimens were used to evaluate the relaxation behavior of these tissues in bulge inflation conditions. After five volume increments, reaching initial pressure levels comparable with those which have been chosen for MCM observations, pressure-time curves were recorded. All curves show a common trend that was described as exponential decays (Fig. 5). The average and standard deviation of the lifetime parameters of the 4 specimens for each initial pressure level are reported in Table 2. They were used as guidelines for the bulge inflation protocol in the MCM.

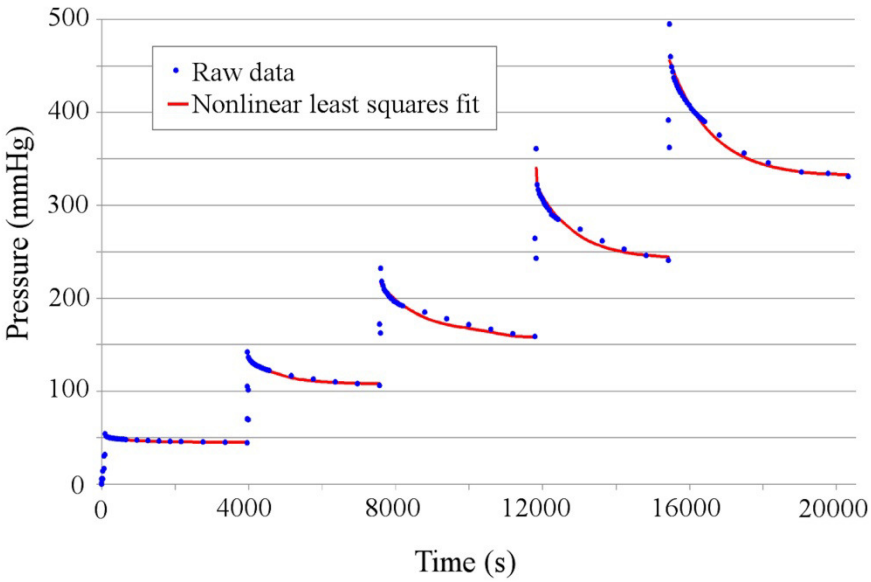

Fig. 5 Quantification of the pressure relaxation behavior. Representative curves of one out of four tested porcine aortic segments inflated over a range of 0–500 mmHg. Each curve was fitted with an exponential decay equation.

Table 2 Quantified relaxation lifetime given as average and standard deviation with n=4 at 5 pressure steps.

Initial pressure P_0 (mmHg)	**50**	**150**	**250**	**350**	**500**
Mean lifetime τ (s)	577 ± 41	818 ± 68	1021 ± 151	1064 ± 196	1146 ± 249

3.2. 3D visualization in aortic adventitia

Following the previous results, the stabilization period imposed between the inflation and the 3D scans with the MCM was set at 15–20 min.

The post processing slice matching program through 2D inter-correlation (see section 2.5.1) permitted then to quantify the motion along the radial direction (or z direction) of each 3D stack, and correct the interslice distances. The average percentage change between the estimated interslice distance and the z-step of the 3D acquisition for all specimens independently of the category were: 16.4 ± 26.5 % at 0 mmHg (25 stacks, 14 specimens), − 12.6 ± 19.3 % at 200 mmHg (21 stacks, 13 specimens), and − 1.5 ± 18.9 % at 450 mmHg (12 stacks, 7 specimens). A positive value indicates an increase of the interslice distance after the correction. Some stacks are missing because their intercorrelation coefficients were below the quality threshold.

On the basis of this additional information, the thickness of all the stacks was revised prior to further analysis. Fig. 6 (a, b, c) show the 3D representation of three representative specimens in two different pressure states.

In a qualitative analysis we note that the typical collagen dense network architecture in the adventitia with undulated collagen fiber bundles was highly distinctive in the unloaded state. A feature of most of the observed porcine collagen architectures was that they exhibited a more marked degree of fiber crimping compared to human specimens. Inflation led to the uncrimping of the fibers, which was nearly complete at 200 mmHg and no longer created ripples at 450 mmHg. Collagen fibers were organized in thick bundles at 0 mmHg which tended to separate into a network of thinner bundles at high pressures. Direction and shape of the collagen fibers were often difficult to distinguish when unloaded fibers are crimped. On the other hand, collagen fibers produced stronger SHG signals when pressure and uncrimping increased, so their direction was more apparent. In this state, we could recognize in almost all specimens collagen fibers in a diagonal

direction, as well as in the axial direction. Fibers in circumferential direction were seen less frequently.

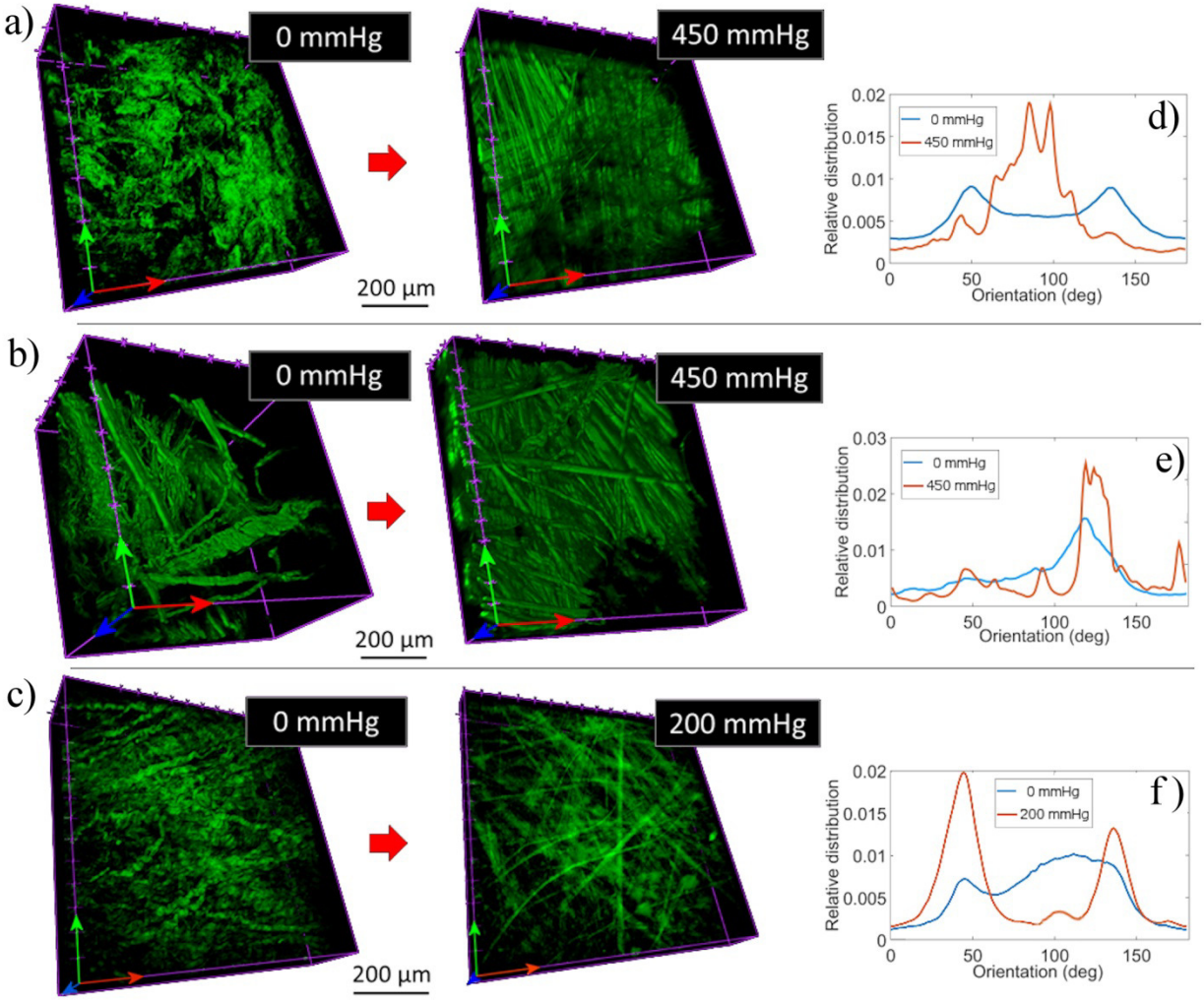

Fig. 6 Representative MCM 3D images of collagen fibers (SHG channel) at different values of pressure after stack-specific z-motion correction and respective orientation histograms. Green, red and blue arrows indicate axial, circumferential and radial directions, respectively. (a) Porcine aorta, thoracic descending part. (b) Non-aneurysmal human aorta: 71 year old female, thoracic descending part, calcified tissue. (c) Aneurysmal human aorta: 63 year old female, thoracic ascending part. (d, e, f) Average planar orientation of each of the previous 3D images at different value of pressure. (For interpretation of the references to color in this figure legend, the reader is referred to the web version of this article.)

Elastin fibers were rarely present in images. When they were present, their conformation varied less than collagen during the inflation, as they appeared to be less crimped at 0 mmHg. The TPF signal originated mainly from fluorescent dust present on the surface and collagen fibers.

3.3. Continuous planar orientation of collagen fibers

Fig. 6 (d, e, f) show representative average orientation histograms calculated by using OrientationJ. Then, quantification of the orientation of the fibers was made by fitting the histograms with the 4-family fitting procedure. These families were ranked according to their contribution to the global distribution for each specimen. Fig. 7 shows the orientations of families with a contribution exceeding 20%. Initially, most collagen fibers were mainly oriented at approximately 45° and 135° with respect to the axial-circumferential plane. Some components were aligned along the axial direction (approximately 90°). Moreover, results at 200 mmHg and 450 mmHg did not yield to any evident reorientation of the fibers under stretching. Similar results were obtained in all three categories of tissues. This trend is very different from the pronounced fiber alignment commonly observed during uni-axial tests (Hill et al., 2012) and likely to be due to the biaxial loading in this experiment. It suggests that re-orientation is marginal in aneurysmal conditions.

In addition, the AI and DI exhibited clear trends: The average initial values at 0 mmHg of AI (multiplied by factor 10^{-3}) are 3.6 ± 1.4, 3.8 ± 0.8 and 4.2 ± 2.2 and of DI are 38.1 ± 20.9, 39.5 ± 1.0 and 18.3 ± 9.1, respectively, in porcine, non-aneurysmal human and human ATAA specimens. With increasing pressure AI had an increasing trend and the DI has a decreasing trend. Table 3 gives a summary of the variation of these indices with respect to the values at 0 mmHg. The evolution of AI is probably linked to the progressive uncrimping and straightening of collagen fibers during the inflation. Besides, there is a reduction of the dispersion in fiber orientation indicated by the negative evolution of DI; in fact, a high base area means fibers spread evenly across the orientation range.

Initial values of AI suggest that, at zero-pressure state, adventitia fibers were generally straighter in humans – especially in ATAA – than in pigs.

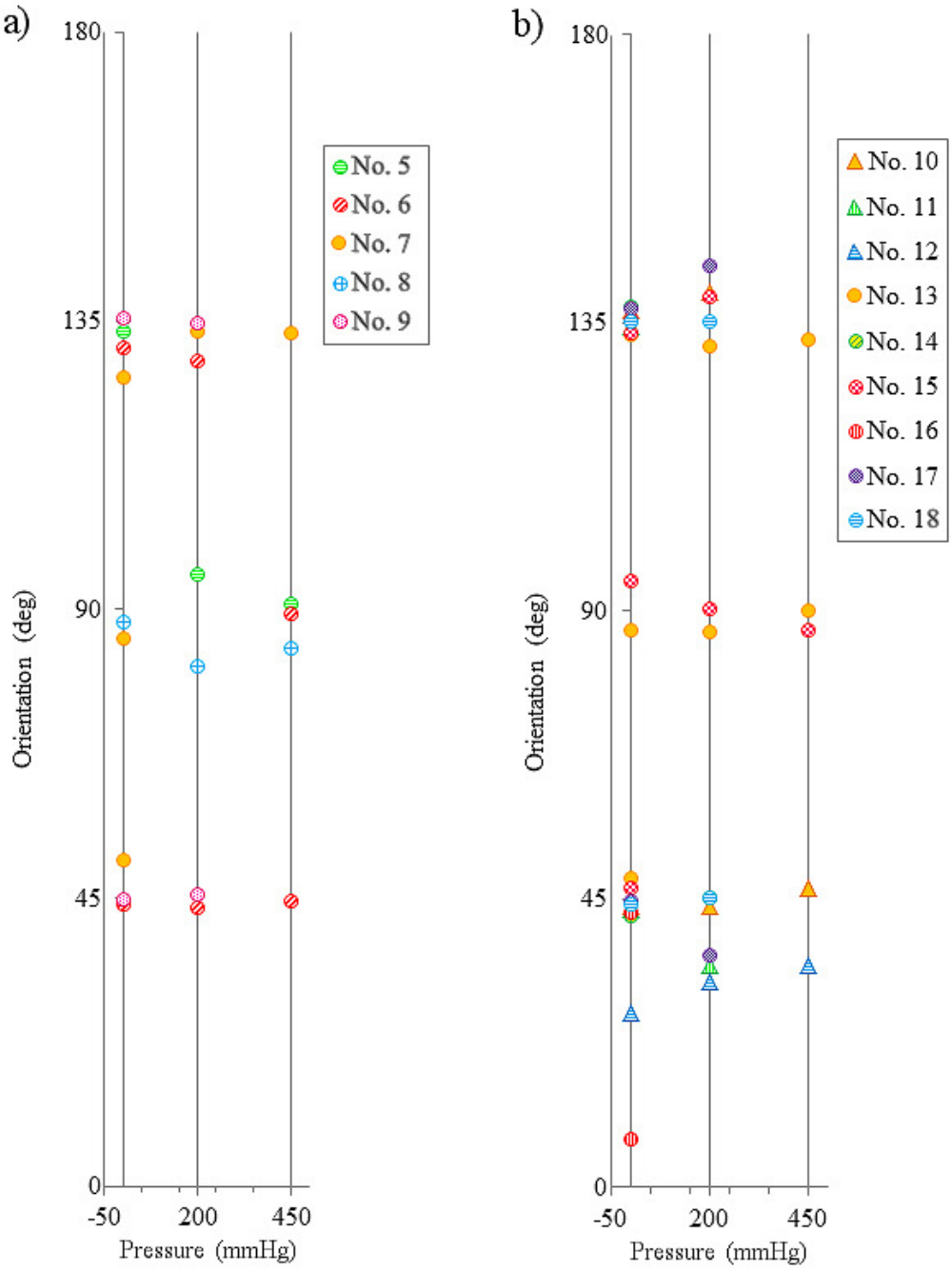

Fig. 7 Mean value of orientation (θ_m) of the families whose contribution is larger than 20% found in all the scanned 3D images. The orientations 0° and 90° indicate the circumferential and axial directions of the aorta. (a) Results of porcine specimens and (b) results of non-aneurysmal human (triangular markers) and ATAA specimens (circular markers) at different inflated pressure.

Table 3 Percentage differences between initial values at 0 mmHg of AI and DI and the values at 200 mmHg and 450 mmHg. The three categories of tissue have been distinguished		
Porcine specimens (n = 5)		
	Δ AI %	Δ DI %
200mmHg	66.9 ± 63.1	-29.0 ± 31.3
450mmHg	105.4 ± 86.1	-44.8 ± 30.3
Non-aneurysmal human specimens (n = 3)		
	Δ AI %	Δ DI %
200mmHg	78.8 ± 79.2	-24.9 ± 16.3
450mmHg	97.2 ± 116.6	-25.3 ± 19.5
Human ATAA specimens (n = 6)		
	Δ AI %	Δ DI %
200mmHg	10.6 ± 19.5	-41.7 ± 18.1
450mmHg	24.2 ± 29.6	-63.0 ± 23.3

Taking also into account the variation with the pressure, the initial more marked crimping of porcine fibers and non-aneurysmal human fibers has led to a sharper straightening at high pressures compared to what happens in ATAA specimens. The percentage differences between pressurized states and zero pressure were indeed much less for ATAA specimens than non-aneurysmal and porcine specimens. The Dispersion Index values suggest that fiber orientations were also less dispersed in human aneurysm wall tissue. In addition, its percentage difference shows that this trend was more marked when the specimens were inflated. In brief, the evolution of the two indices and the absence of evidence of reorientation of the main mean angles indicate that fibers tended to tense in the directions in which they were initially oriented.

In addition to the assessment and quantification of the average orientation distribution of the entire stack, also the local collagen fiber orientations in each slice were available. Moreover, the z-motion balancing was applied to the analyzed stacks to have a reliable value of the radial positions data. Three-dimensional intensity plots of the orientations (Fig. 8) confirm the resulting average orientations of approx. 45/90/135° and offer further proof that no reorientation has clearly taken

place during the inflation test. In addition, it is possible to observe that without any applied pressure thin individual fiber bundles were present on the surface of the adventitia. These fibers were disorganized, and took up a large portion of the observable volume. With the increasing pressure, visible fibers got nearer to each other, since the same orientation peaks were less spread out in the z axis at higher pressures. The straightening increased and the dispersion decreased with the pressure, since the orientation peaks are more isolated (clearly visible in Fig. 8, 200mmHg), with higher values, and lower surrounding values. From the results of all specimens (not shown here) no specific orientation order was found through the thickness. It can be noticed that histograms of deepest slices showed a tendency to detect orientations at 45° and 135° whereas no orientation was recognizable by eye. It was checked that these contributions in the distribution were at least 50% lower than peaks due to recognizable structures and never caused a wrong interpretation of the mean values of orientation.

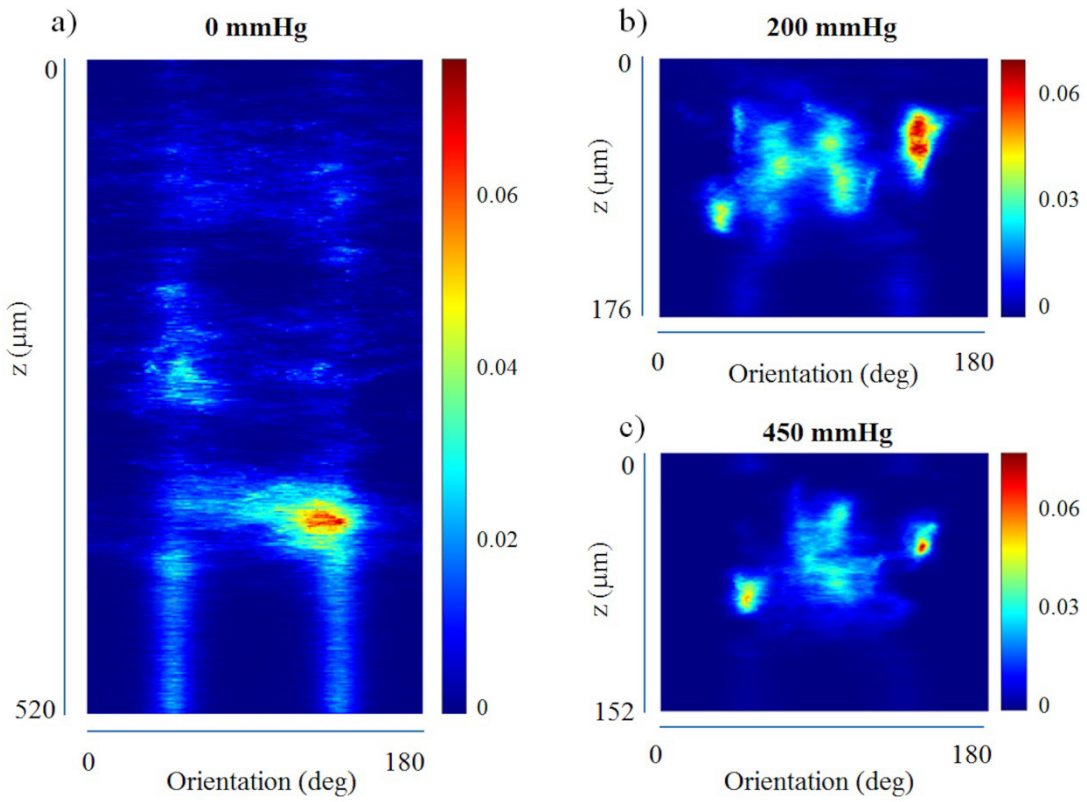

Fig. 8 Intensity plots of the orientation of a set of collagen fibers through the acquired thickness at 0 (a), 200 (b) and 450 mmHg (c). Vertical and horizontal axes indicate the z position and the

orientation, respectively. The color map indicates the distribution of orientation calculated for each slice, with global division by the maximum value within the stack. Representative results of aneurysmal human aorta, 61 year old female, thoracic ascending part. (For interpretation of the references to color in this figure legend, the reader is referred to the web version of this article.)

4. Discussion

This paper introduces an original experimental method to provide biaxial loading conditions close to *in vivo* conditions, involving a bulge inflation test coupled with multi-photon confocal microscopy to investigate the 3D microarchitecture of the principal structural proteins of the aortic wall. Only few previous studies have presented a combination of a bulge inflation test with a MCM technique. They were performed on tissues different from ours, i.e. on liver membrane (Bircher et al., 2017; Jayyosi et al., 2016) and corneal tissue (Benoit et al., 2016). In addition, the samples used in these studies were smaller than aortic specimens and the applied pressure did not reach the level of typical aortic pressures. Moreover, the thin thickness of the cornea and liver membrane allowed imaging the whole thickness of the specimens, which was impossible to achieve with the porcine and human aortic tissues, The presented experimental approach has been designed to permit a high degree of stability under the MCM and was completed by innovative post-processing steps necessary to compensate artefacts or motions in the laser beam direction. Indeed, for a thick soft tissue at this scale and this pressure magnitude, any kind of motion may produce important distortions in the 3D acquisitions. We combined different acquisition and processing methods to obtain a stable automatic three-dimensional analysis of the collagen fiber microstructure of thick aortic adventitial tissues.

In the first instance we observed a significant decay of the pressure of the system during the inflation, even if no evidence of water losses has been recorded through the hermetic structure and no evidence of microstructural deformation could be observed on the images. We verified that this

situation was associated with a visible motion of the tissue, particularly in the z axis. Such behavior could depend on the conjunction of several factors, linked to the inflation device or due to the viscoelasticity of the inflated tissue. In the first case, a relaxation of the water pipe should for example be considered. In the latter case, the hypothesis of an effect of internal fluid flow and long-term stress relaxation of the tissue could be made, confirming observations on biological tissues made by other groups (Mauri et al., 2015). To the best of our knowledge, no other study that coupled mechanical tests and microscopical 3D imaging reported a correction technique. As a consequence, in this context, 3D imaging techniques such as MCM cannot really give reliable 3D images. Hence 2D projections are most often used (Krasny et al., 2017; Rezakhaniha et al., 2012). To address this issue, we proposed a three-step procedure: the definition of a stabilization period, a compound image acquisition and a post-processing z correction through 2D image correlation. A Fourier method was chosen since these methods for image registration are robust in case of correlated noise and frequency dependent noise. It allowed to get a reliable corrected interslice distance in the majority of cases, even in the presence of small water leakages. In fact, the resulted estimated interslice distances generally indicated widely varying movements of the tissue, in both magnitude and direction.

The morphology of the observed tissues is complex and heterogeneous because of the thickness and microstructural variability within the porcine and human aortic tissues, especially in the case of conditions such as thoracic aortic aneurysms. There is a relatively high number of experimental studies in the literature which report the collagen content and architecture in human aorta and in case of aortic aneurysms and dissections under polarized light (De Figueiredo Borge et al., 2008; Gasser et al., 2012) or MCM (Tsamis et al., 2016). They reported ribbon-like collagen in healthy adventitial layer and, in general, disturbances or absence of the normal collagen fibril organization when the tissue is associated with the mentioned arteropathies (Lindeman et al., 2010; Tsamis et al., 2013). Currently, only few of these studies were conducted to ascertain the 3D microstructure of

adventitial fibers. In the latter case, they often involved fixed and embedded tissues or tissues undergoing optical clearing under a transmural pressure (Schriefl et al., 2013). However, all studies carried out on this subject presented results based only on few specimens, with a small field of view.

Using the proposed method, we could analyze the 3D structure and automatically quantify collagen fiber planar orientation and straightness of 5 porcine, 3 human normal, and 6 human aneurysm specimens under bulge inflation. From the experimental data, we used a generic convolution of Gaussian functions describing 4 families of fibers in which parameters can be used to evaluate the mean angles of the fibers and identify two indices of alignment and dispersion. Our finding of orientation confirmed the similarity between human and porcine morphology, in agreement with the qualitative observations. Quantification of the orientations as a ranking of the parameters indicated in most cases 3 principal angles 45/135/90°. At zero pressure state, fiber alignment is more pronounced in human specimens than in porcine specimens and fiber dispersion in the entire orientation field, which indicates the extent of isotropy, is less pronounced in aneurysmal adventitia. No measurable reorientation could be acknowledged during this inflation test. Our data lead to propose that alignment and anisotropy increase during pressurization similarly for the three categories of tissues but fiber bundles do not exhibit the same level of crimping at zero pressure state, with the porcine ones being more undulated. This observation may be due to a difference between species or age (pigs were young and human donors old). Unfortunately, no specimen was available to make paired comparison on age and confirm this hypothesis.

Previous studies of collagen fibers orientation in adventitia of aorta and other vessels showed controversial results, due to differences in the mechanical boundary conditions, but we found a good agreement with many recent reports. Rezakhaniha et al. (2012) studied the orientation and the waviness of collagen in adventitia of cut-open fresh rabbit carotid arteries. They reported four mean directions of 0°, 90°, 47° and 137° with respect to the circumferential axis of the vessel. Sugita and

Matsumoto (2016) found a prominent number of fibers oriented along the longitudinal direction in the external layer of fresh rabbit and mouse aortae. For tubular segments of aorta pressurized under MCM, they observed an organization which had our trends of alignment and dispersion during the pressurization. Schriefl et al. (2012; 2013) investigated the collagen architecture in fixed tubular human aorta. Two fiber families were observed at approximately 45° and − 45° in adventitia, and a preferred longitudinal orientation in the deeper part of the adventitia was reported. Schrauwen et al. (2012) reported changes in alignment similar to what we observed in inflated rabbit carotid artery segments and a symmetrical distribution around the axial direction at approximately ± 70°. Two families with diagonal orientations were described also by Nierenberger et al. (2015) in jugular porcine vein adventitia.

The orientation maps through the z direction of the stacks after the application of the z-motion correction permitted to also evaluate the 3D disposition of the fibers along the thickness. They confirmed what we observed through the use of the average orientations, with a significant inter-specimen variability and no specific intra-specimen variability over the thickness of the specimens.

An innovative aspect of the present study was the capacity to follow continuously the same set of fibers during all the protocol of pressurization and stabilization and then report the evolution of the orientation distribution without any dependence of different regions. The proposed methodology has also the advantage to be completely automated: quantitative analysis could be computed for each acquired slice and no bias and no rough sampling due to manual measurements was possible. Including the corrected interslice values, these 3D images could be exploited more effectively, calculating not only planar parameters but using the radial information to investigate 3D parameters, which will be further investigated in the future. Additionally, this setup is suitable and will be used, in the future, for analysis of the adventitial structure submitted to over pressurization in order to study pre-rupture states.

Some limitations in the method of the present study should be acknowledged.

Although the bulge inflation testing method has many advantages over uniaxial and planar biaxial tests, it does not preserve the native geometry of the specimens, which could lead to microarchitecture alterations. On the other hand, compared to whole-body inflation tests of arterial segments, this method does not require long aortae segments, which are particularly difficult to obtain from aneurysm repair.

The MCM results were obtained for a limited surface area of about 1.1 mm^2. Two adjacent regions were taken into consideration for each specimen, and the analyses of the histograms reveal low variability between the neighboring fibers. This remains one of the main limitations of MCM techniques. We also have to consider the limited number of specimens and especially human non-aneurysmal specimens which, at present, limit our conclusions on those.

We analyzed the planar collagen fiber orientation using only the 2D data, assuming that the fibers are mainly lying in the circumferential-longitudinal plane. This choice facilitated the calculation but in the future out-of-plane contribution should be considered. Moreover, it was noted from the orientation maps through the thickness that OrientationJ, used with MCM images with the chosen set of parameters (see Section 2.3 and 2.5.2), had a tendency to find orientation peaks at 45° and 135° when there was no defined shape in a slice. These peaks were, however, significantly low in all intensity plots and their weight did not allow establishing main mean orientations in the stacks.

5. Conclusions

This study presents a stable automatic 3D analysis of human and porcine adventitial collagen microstructure under biaxial loads that closely mimicked physiologic loading conditions. The reliability of 3D data was ensured by definition of a stabilization period coupled with an innovative z-motion correction method. Continuous 3D observations allowed ROI tracking all along the test. The results showed the existence of 3 predominant collagen fibers orientations at zero-pressure load

and increasing inflation pressure. No evident reorientation trend of the fibers was reported. The analysis of the orientation distribution revealed the progressive uncrimping and straightening of collagen bundles, and their decreasing dispersion of orientation. Moreover it permitted to observe different initial states and evolutions in porcine and human aortae, especially in ATAA. In fact, an initial more marked crimping of porcine and non-aneurysmal fibers led to a sharper straightening at high pressures compared to ATAA specimens which showed less pronounced changes. These findings provide further insight into the micro-architectural changes within the arterial wall and encourage to further comparison of aneurysmal and non-aneurysmal tissues.

Acknowledgment

This work was funded by the European Research Council, Starting Grant no. 638804, AArteMIS.

References

Benoit A., Latour G., Marie-Claire S.K. and Allain J.M., Simultaneous microstructural and mechanical characterization of human corneas at increasing pressure, J. Mech. Behav. Biomed. Mater. 60, 2016, 93–105, http://dx.doi.org/10.1016/j.jmbbm.2015.12.031.

Bircher K., Ehret A.E. and Mazza E., Microstructure based prediction of the deformation behavior of soft collagenous membranes, Soft Matter 2017, http://dx.doi.org/10.1039/c7sm00101k.

Boulesteix T., Pena A.M., Godeau G., Sauviat M.P., Beaurepaire E. and Schanne-Klein M.C., Micrometer scale ex vivo multiphoton imaging of unstained arterial wall structure, Cytometry Part A 69 (1), 2006, 20–26, http://dx.doi.org/10.1002/cyto.a.20196.

Chandran P.L. and Barocas V.H., Affine versus non-affine fibril kinematics in collagen networks: theoretical studies of network behavior, J. Biomed. Eng. 128 (2), 2006, 259–270, http://dx.doi.org/10.1115/1.2165699.

Chow M.J., Turcotte R., Lin C.P. and Zhang Y., Arterial extracellular matrix: a mechanobiological study of the contributions and interactions of elastin and collagen, Biophys. J. 106 (12), 2014, 2684–2692, http://dx.doi.org/10.1016/j.bpj.2014.05.014.

De Figueiredo Borges L., Jaldin R.G., Dias R.R., Stolf N.A.G., Michel J.B. and Gutierrez P.S., Collagen is reduced and disrupted in human aneurysms and dissections of ascending aorta, Hum. Pathol. 39 (3), 2008, 437–443, http://dx.doi.org/10.1016/j.humpath.2007.08.003.

Duprey A., Trabelsi O., Vola M., Favre J.P. and Avril S., Biaxial rupture properties of ascending thoracic aortic aneurysms, Acta Biomater. 42, 2016, 273–285, http://dx.doi.org/10.1016/j.actbio.2016.06.028.

Gasser T.C., Ogden R.W. and Holzapfel G.A., Hyperelastic modelling of arterial layers with distributed collagen fibre orientations, J. R. Soc. Interface 3 (6), 2006, 15–35, http://dx.doi.org/10.1098/rsif.2005.0073.

Gasser T.C., Gallinetti S., Xing X., Forsell C., Swedenborg J. and Roy J., Spatial orientation of collagen fibers in the abdominal aortic aneurysm's wall and its relation to wall mechanics, Acta Biomater. 8 (8), 2012, 3091–3103, http://dx.doi.org/10.1016/j.actbio.2012.04.044.

Helfenstein-Didier C., Taïnoff, D., Viville, J., Adrien, J., Maire, E., Badel, P., 2016. In situ tensile tests of medial arterial tissue in X-ray microtomography. In: Proceeding of 22nd Congress of the European Society of Biomechanics (ESB 2016), Jul 2016, Lyon, France. ⟨https://esbiomech.org/conference/index.php/congress/lyon2016/paper/viewFile/822/460⟩ (Accessed 5 May 2017).

Hemmasizadeh A., Tsamis A., Cheheltani R., Assari S., D'Amore A., Autieri M., Kiani M.F., Pleshko N., Wagner W.R., Watkins S.C., Vorp D.A. and Darvish K., Correlations between transmural mechanical and morphological properties in porcine thoracic descending aorta, J. Mech. Behav. Biomed. 47, 2015, 12–20, http://dx.doi.org/10.1016/j.jmbbm.2015.03.004.

Hill M.R., Duan X., Gibson G.A., Watkins S. and Robertson A.M., A theoretical and non-destructive experimental approach for direct inclusion of measured collagen orientation and recruitment into mechanical models of the artery wall, J. Biomech. 45 (5), 2012, 762–771, http://dx.doi.org/10.1016/j.jbiomech.2011.11.016.

Holzapfel G.A., Gasser T.C. and Ogden R.W., A new constitutive framework for arterial wall mechanics and a comparative study of material models, J. Elast. 61 (1-31–3), 2000, 1–48, http://dx.doi.org/10.1023/A:1010835316564.

Iliopoulos D.C., Deveja R.P., Kritharis E.P., Perrea D., Sionis G.D., Toutouzas K. and Sokolis D.P., Regional and directional variations in the mechanical properties of ascending thoracic aortic aneurysms, Med. Eng. Phys. 31 (1), 2009a, 1–9, http://dx.doi.org/10.1016/j.medengphy.2008.03.002.

Iliopoulos D.C., Kritharis E.P., Giagini A.T., Papadodima S.A. and Sokolis D.P., Ascending thoracic aortic aneurysms are associated with compositional remodeling and vessel stiffening but not weakening in age-matched subjects, J. Thorac. Cardiovasc. Surg. 137 (1), 2009b, 101–109, http://dx.doi.org/10.1016/j.jtcvs.2008.07.023.

Jayyosi C., Coret M. and Bruyere-Garnier K., Characterizing liver capsule microstructure via in situ bulge test coupled with multiphoton imaging, J. Mech. Behav. Biomed. Mater. 54, 2016, 229–243, http://dx.doi.org/10.1016/j.jmbbm.2015.09.031.

Koch R.G., Tsamis A., D'Amore A., Wagner W.R., Watkins S.C., Gleason T.G. and Vorp D.A., A custom image-based analysis tool for quantifying elastin and collagen micro-architecture in the wall of the human aorta from multi-photon microscopy, J. Biomech. 47 (5), 2014, 935–943, http://dx.doi.org/10.1016/j.jbiomech.2014.01.027.

Krasny W., Morin C., Magoariec H. and Avril S., A comprehensive study of layer-specific morphological changes in the microstructure of carotid arteries under uniaxial load, Acta Biomater. 2017, http://dx.doi.org/10.1016/j.actbio.2017.04.033.

Länne T., Sonesson B., Bergqvist D., Bengtsson H. and Gustafsson D., Diameter and compliance in the male human abdominal aorta: influence of age and aortic aneurysm, Eur. J. Vasc. Endovasc. Surg. 6 (2), 1992, 178–184, http://dx.doi.org/10.1016/S0950-821X(05)80237-3.

Lindeman J.H., Ashcroft B.A., Beenakker J.W.M., van Es M., Koekkoek N.B., Prins F.A. and Oosterkamp T.H., Distinct defects in collagen microarchitecture underlie vessel-wall failure in advanced abdominal aneurysms and aneurysms in Marfan syndrome. Proc. Natl. Acad. Sci. U. S. A., 107 (2), 2010, 862-865, http://dx.doi.org/10.1073/pnas.0910312107.

Marra S.P., Kennedy F.E., Kinkaid J.N. and Fillinger M.F., Elastic and rupture properties of porcine aortic tissue measured using inflation testing, Cardiovasc. Eng. 6 (4), 2006, 123–131, http://dx.doi.org/10.1007/s10558-006-9021-5.

Mauri A., Perrini M., Ehret A.E., De Focatiis D.S. and Mazza E., Time-dependent mechanical behavior of human amnion: macroscopic and microscopic characterization, Acta Biomater. 11, 2015, 314–323, http://dx.doi.org/10.1016/j.actbio.2014.09.012.

Mohan D. and Melvin J.W., Failure properties of passive human aortic tissue. II—Biaxial tension tests, J. Biomech. 16 (1), 1983, 3139–3744, http://dx.doi.org/10.1016/0021-9290(83)90044-1.

Nierenberger M., Fargier G., Ahzi S. and Rémond Y., Evolution of the three-dimensional collagen structure in vascular walls during deformation: an in situ mechanical testing under multiphoton microscopy observation, Biomech. Model. Mechanobiol. 14 (4), 2015, 693–702, http://dx.doi.org/10.1007/s10237-014-0630-4.

Niestrawska J.A., Viertler C., Regitnig P., Cohnert T.U., Sommer G. and Holzapfel G.A., Microstructure and mechanics of healthy and aneurysmatic abdominal aortas: experimental analysis and modelling, J. R. Soc. Interface 13 (124), 2016, 20160620, http://dx.doi.org/10.1098/rsif.2016.0620.

O'Connell M.K., Murthy S., Phan S., Xu C., Buchanan J., Spilker R., Dalman R.L., Zarins C.K., Denk W. and Taylor C.A., The three-dimensional micro-and nanostructure of the aortic medial lamellar unit measured using 3D confocal and electron microscopy imaging, Matrix Biol. 27 (3), 2008, 171–181, http://dx.doi.org/10.1016/j.matbio.2007.10.008.

Püspöki Z., Storath M., Sage D. and Unser M., Transforms and operators for directional bioimage analysis: a survey, Adv. Anat. Embryol. Cell Biol. 219, 2016, 69–93, http://dx.doi.org/10.1007/978-3-319-28549-8_3.

Rezakhaniha R., Agianniotis A., Schrauwen J.T., Griffa A., Sage D., Bouten C.V.C., van de Vosse F.N., Unser M. and Stergiopulos N., Experimental investigation of collagen waviness and orientation in the arterial adventitia using confocal laser scanning microscopy, Biomech. Model. Mechanobiol. 11 (3), 2012, 461–473, http://dx.doi.org/10.1007/s10237-011-0325-z.

Romo A., Badel P., Duprey A., Favre J.P. and Avril S., In vitro analysis of localized aneurysm rupture, J. Biomech. 47 (3), 2014, 607–616, http://dx.doi.org/10.1016/j.jbiomech.2013.12.012.

Schrauwen J.T.C., Vilanova A., Rezakhaniha R., Stergiopulos N., Van De Vosse F.N. and Bovendeerd P.H.M., A method for the quantification of the pressure dependent 3D collagen configuration in the arterial adventitia, J. Struct. Biol. 180 (2), 2012, 335–342, http://dx.doi.org/10.1016/j.jsb.2012.06.007.

Schriefl A.J., Zeindlinger G., Pierce D.M., Regitnig P. and Holzapfel G.A., Determination of the layer-specific distributed collagen fibre orientations in human thoracic and abdominal aortas and common iliac arteries, J. R. Soc. Interface 9, 2012, 1275–1286, http://dx.doi.org/10.1098/rsif.2011.0727.

Schriefl A.J., Wolinski H., Regitnig P., Kohlwein S.D. and Holzapfel G.A., An automated approach for three-dimensional quantification of fibrillar structures in optically cleared soft biological tissues, J. R. Soc. Interface 10 (80), 2013, 20120760, http://dx.doi.org/10.1098/rsif.2012.0760.

Spronck B., Megens R.T., Reesink K.D. and Delhaas T., A method for three-dimensional quantification of vascular smooth muscle orientation: application in viable murine carotid arteries, Biomech. Model. Mechanobiol. 15 (2), 2016, 419–432, http://dx.doi.org/10.1007/s10237-015-0699-4.

Sugita S. and Matsumoto T., Multiphoton microscopy observations of 3D elastin and collagen fiber microstructure changes during pressurization in aortic media, Biomech. Model. Mechanobiol. 2016, 1–11, http://dx.doi.org/10.1007/s10237-016-0851-9.

Trabelsi O., Davis F.M., Rodriguez-Matas J.F., Duprey A. and Avril S., Patient specific stress and rupture analysis of ascending thoracic aneurysms, J. Biomech. 48 (10), 2015, 1836–1843, http://dx.doi.org/10.1016/j.jbiomech.2015.04.035.

Tsamis A., Krawiec J.T. and Vorp D.A., Elastin and collagen fibre microstructure of the human aorta in ageing and disease: a review, J. R. Soc. Interface 10 (83), 2013, 20121004, http://dx.doi.org/10.1098/rsif.2012.1004.

Tsamis A., Phillippi J.A., Koch R.G., Chan P.G., Krawiec J.T., D'amore A. and Gleason T.G., Extracellular matrix fiber microarchitecture is region-specific in bicuspid aortic valve-associated ascending aortopathy, J. Thorac. Cardiovasc. Surg. 151 (6), 2016, 1718–1728, http://dx.doi.org/10.1016/j.jtcvs.2016.02.019.

Voytik-Harbin S.L., Rajwa B. and Robinson J.P., Three-dimensional imaging of extracellular matrix and extracellular matrix-cell interactions, Methods Cell Biol. 63, 2001, 583–597, http://dx.doi.org/10.1016/S0091-679X(01)63031-0.

Walton L.A., Bradley R.S., Withers P.J., Newton V.L., Watson R.E., Austin C. and Sherratt M.J., Morphological characterization of unstained and intact tissue micro-architecture by X-ray computed micro-and nano-tomography, Sci. Rep. 2015, 5, http://dx.doi.org/10.1038/srep10074.

Appendix A. Z-motion correction method

See appendix Fig. A.1 here.

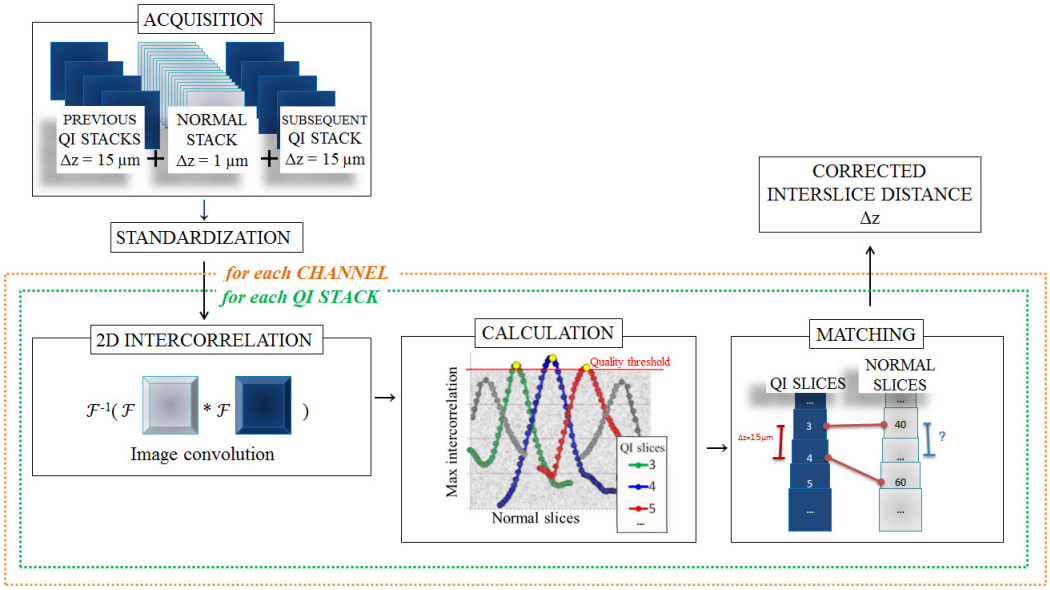

Fig. A.1 Conceptual framework for calculating z-motion values.

The acquisition of each normal stack took in general 15-30 min and possible motion effects had to be addressed on the basis of the relaxation related behavior analysis described in Section 2.2. The quantification and correction of mechanical rigid motions within the 3D stack of images in the direction of the z-coordinate was performed according to the following.

Regarding the experimental acquisition protocol, one quasi-instantaneous (QI) stack was recorded immediately before each normal stack and another QI stack was recorded immediately after each normal stack. The distance between the slices of the QI stack was 15 µm and it was considered unaffected since the instrument acquisition time was set to a minimum (total duration of less than 30 s).

Regarding the post-processing correction, we considered one QI stack and one channel at a time. The z-motion correction method was structured as follow:

- All scanned slices – quasi-instantaneous and normal – were standardized by subtraction of the mean grey level of the image and division by its standard deviation.
- The 2D Fast Fourier Transforms of each QI slice were calculated and multiplied by the 2D Fast Fourier Transform of each normal slice. The maximum of the inverse Fast Fourier Transform of the product was taken as Intercorrelation Coefficient (IC). The IC indicated a measure of similarity between one QI slice and one normal slice.
- The highest IC of each QI slice indicated the best matching normal slice. The index of this normal slice within the normal stack was recorded as Intercorrelation Index (II).
- The overall maximum IC value was multiplied by 0.8 and used as quality threshold: only the combinations with a coefficient greater than or equal to this threshold were considered in the following. The quality threshold value was chosen so as to ensure a number of slice combinations sufficient for the calculation.
- When this condition was fulfilled, the differences between the corresponding sequential II in seamless sequences were calculated: these differences indicated the distance in µm between 2 planes in the normal stack which were, in reality, 15 µm far from each other in the QI stack. The resulting values were averaged and the standard deviation was calculated.

This process was repeated for both stacks of channel 0 and channel 1, and for both the previous and subsequent QI scans. Then the estimated interslice distance Δz was calculated as a weighted average of all obtained results:

Equation A.1

$$w_{ik} = \frac{1}{sd_{ik}} N_{ik} \qquad i = 0,1 \qquad k = a, b$$

Equation A.2

$$\Delta z(\mu m) = 15 / \left[\left(\frac{(m_{1a} * w_{1a}) + (m_{0a} * w_{0a})}{w_{1a} + w_{0a}} + \frac{(m_{1b} * w_{1b}) + (m_{0b} * w_{0b})}{w_{1b} + w_{0b}} \right) / 2 \right]$$

w_{ik} is the weight of the result for channel i compared to QI scan k, *sd* represents the standard deviation, *m* is the average and *N* is the number of slices satisfying the quality threshold. The index *i* indicates the channel 0 or 1, the index k indicates the combination between the normal stack and the previous QI stack (a) or the subsequent QI stack (b).